EXPERIMENTAL STUDY OF THE WAKE OF A SIMPLIFIED TRUCK MODEL IN GROUND PROXIMITY IN VIEW OF DEFINING A CONTROL STRATEGY FOR DRAG REDUCTION

M. Szmigiel, M. Michard, T. Castelain, D. Juvé, D. Chacaton

52nd 3AF International Conference on Applied Aerodynamics
27 – 29 March 2017, Lyon – France

FP09-AERO2017-szmigiel

EXPERIMENTAL STUDY OF THE WAKE OF A SIMPLIFIED TRUCK MODEL IN GROUND PROXIMITY IN VIEW OF DEFINING A CONTROL STRATEGY FOR DRAG REDUCTION

M. SZMIGIEL[1,2], M. MICHARD[1], T. CASTELAIN[1], D. JUVE[1] and D. CHACATON[2]
[1]*LMFA UMR 5509, 36 Av. Guy-de-Collongue, Ecully, FRANCE, mathieu.szmigiel@doctorant.ec-lyon.fr*
[2]*Volvo GTT, Renault Trucks SAS, Cab Engineering Lyon, 99 route de Lyon, Saint-Priest, France*

ABSTRACT

Near wake study of a simplified truck model is presented for various underbody velocity. The mean base pressure evolution and the near wake structure evolution for a change of the underbody velocity lead to the identification of four classes of flow. The wake of class (I), for underbody velocities below 15% of the free stream velocity U_∞ looks like a 3D backward facing step. Then for higher underbody velocities, until typically $0.4U_\infty$, the wakes of classes (II) and (III) are associated to a back-flow impaging the rear base. This back-flow is responsible for a low pressure area on the bottom of the rear base. It would then be interesting to limit the curvature of the back-flow in order to limit the low pressure. The last class is identified for an underbody velocity above $0.6U_\infty$ and the wake looks like an Ahmed body wake. For all classes, turbulence is mainly localized in the upper and lateral shear layers. Flow control on these sides would be useful to attenuate these velocity fluctuations for stabilizing the near wake.

1. INTRODUCTION

The near-wake of medium and heavy duty vehicles is different from the wake of passenger cars because of (i) an aspect ratio H/W between height H and width W of the trailer above one and (ii) a large flow obstruction under the trailer, despite a relatively large ground clearance. Flow obstruction results in an underbody velocity U_s much lower than the velocity of the vehicle U_∞, typically in the range between $0.1U_\infty$ to $0.4U_\infty$ depending on the kind of truck and its use.

The well-known Ahmed body [1] with a square-back configuration is usually used to mimic the main features of some road transport vehicles. In the mean sense, this wake consists mainly of a closed recirculation bubble attached to the separation lines of the edges of the trailer rear base. Nevertheless, such a near-wake structure is not representative of real full-scale trailers because the Ahmed body has an aspect ratio H/W below one and the ground clearance G/H is too high to reduce underbody velocity. The Ground Transportation System (GTS) or the Generalized European Transport System (GETS) models have been specifically developed to reproduce the geometric aspect ratio of heavy-duty [12, 17, 22]. However, due to a ground clearance G/H around 0.14, the underbody velocity of these models is similar to U_∞ which finally makes it impossible to reproduce properly the development of the wake observed on vehicles at full scale one [13, 14].

Recently McArthur et al. [15] modified the ground clearance G down to G/H=0.03 on a GTS model. The reduction of G causes a decrease of the underbody velocity as observed by [4, 8, 16] on a square-back Ahmed body. The transition between a wake completely detached from the ground and a wake with a flow separation on the ground is obtained for $G/H \sim 0.14$ for the GTS model. For reduced ground clearance, the authors observe that a mean back-flow is directed from the underbody region toward the rear base or the upper shear layer and is linked to a different distribution of the velocity fluctuations. Nevertheless, this study doesn't allow to associate a base pressure distribution and to clearly identify which parameter is responsible for these modifications: the ground clearance or the value of underbody velocity.

Chaligné et al. [6] have developed a simplified truck model with a specific pressure loss system in the underbody area. The underbody velocity is then equal to $0.1U_\infty$ for a ground clearance $G/H = 0.26$ similar to the ratio on full-scale trailer. For this underbody velocity, the wake in the mid-plane looks like the flow behind a 3D backward facing step. However, the authors have explored just this underbody velocity which does not allow us to know the wake characteristics for higher velocity U_s with the same

ground clearance height.

The aim of the present study is to clarify the impact of the underbody velocity on the near-wake properties and on the base pressure for a square-back geometry of a simplified truck model without changing any geometrical parameters like the ground clearance. The work is organized as follows: the experimental set-up is described in Sec. 2 together with the measurement techniques. Sec. 3 is dedicated to the study of the underbody velocity profiles as a function of the pressure loss intensity. The evolution of the rear base pressure with λ, of the near-wake structures and the turbulence distribution are also discussed in this section. Sec. 4 is dedicated to draw a link between the rear base pressure and the back-flow and Sec. 5 will propose flow control strategies.

2. EXPERIMENTAL SET-UP

2.1 Model

Experiments are conducted in an open-air wind tunnel of 500×500 mm^2 square section. A simplified tractor-trailer model in square-back configuration, presented in Fig. 1, is used. The length L of the bluff body is 320 mm, the height H and the width W of the base are 74 mm and 66 mm respectively. The ground clearance G is 19 mm so the value of $G/H = 0.26$ is identical to that of previous study at larger scale [5] and similar to the value of full scale long haul vehicle. The model is positioned on a flat plate raised from the wind tunnel 133 mm downstream the flat plate leading edge. The free stream velocity U_∞ is set to 25 m/s leading to a Reynolds number based on H with $Re_H = 1.3 \times 10^5$.

The peculiarities of this model are twofold: (i) its aspect ratio $H/W = 1.12$ is greater than unity, contrary to an Ahmed body, to investigate flows around long haul vehicle geometries and (ii) the side skirts are used to channel the underbody flow which is forced to go through a pressure loss system located in the ground clearance, 160 mm downstream the model front. This pressure loss device is made of a 4 mm thick grid with a given porosity, adjustable between 10% to 100% of the ground clearance area. This allows for the underbody velocity to be varied without modifying any geometrical property of the model, *e.g.* the ground clearance height. The characterization of the flow downstream this pressure loss device will be developed in Sec. 3.1. To minimize flow separation on the upstream part of the model, a rounded shape of the model nozzle has been chosen. The choice of the radius for the upper and lateral edges equal to 19 mm and for the lower edge equal to 9 mm is based on results from [5].

The coordinate system is defined as $\vec{x}$ directed toward the flow direction , $\vec{y}$ normal to the ground and $\vec{z}$ forming a direct trihedral. The origin O of the coordinate system is defined as the point on the flat plate at the mid-span and rear end of the model. Velocities u, v and w are respectively associated to the streamwise velocity, the vertical velocity and the horizontal velocity. The time-average, the spatial-average, the fluctuating part and the standard deviation of a are respectively denoted by $\overline{a}$, $\langle a \rangle$, a' and σ_a. The height H, the free-stream velocity U_∞ and the dynamic pressure are used to obtain non-dimensional values marked by an asterisk. Pressures are normalized by the dynamic pressure.

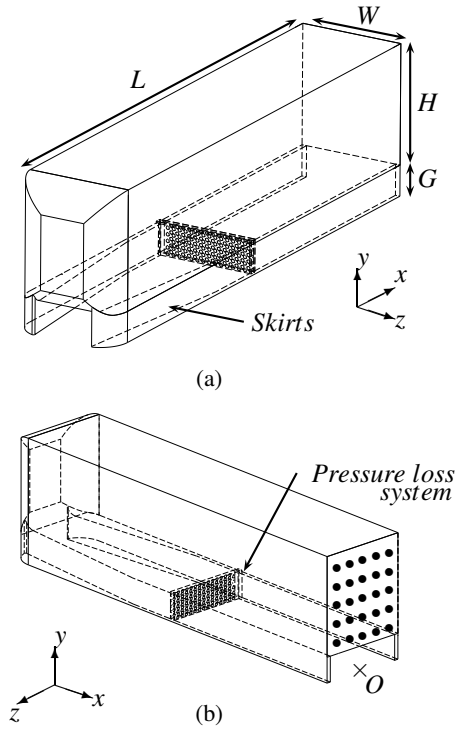

Figure 1: Front view (a) and back view (b) of the model used. Black dots are the static pressure taps and the O sets the origin of the coordinate system.

2.2 Pressure and velocity measurements

The taps are distributed to measure the base pressure with the use of 25 pressure taps (see Fig. 1b). The pressure is measured using a 32-port ESP pressure scanner of ± 1000 Pa full scale. The pressure scanner is linked to each tap by tubes of 270 mm in length and 1/32" inner radius and interfaced to a μDAQ located outside the model. To prevent flow disturbances, communicating wires for data transfers between the pressure scanner and the μDAQ are inserted inside the skirts. During measurements, the acquisition frequency is set to 1 kHz. The frequency response of this set-up has been tested and is found to be in good agreement with the frequency response of a 1/4 IEPE PCB Piezotronics microphone below 400 Hz which is significantly above the frequency of interest here. The upstream static pressure p_0 and ρ the air density are used to define in Eq. 1 a dimensionless pressure coefficient C_p.

$$C_p = \frac{p - p_0}{1/2 \rho U_\infty^2} \tag{1}$$

The whole wake in the mid-plane and the wake in the vertical transversal planes at $x^* = 0.5$ and $x^* = 2$ are characterized by using stereoscopic PIV (SPIV). The laser

system is a Nd:YAG Quantronix Darwin Duo of 2 × 18 mJ . The laser head is situated above the flow. The cameras used are CMOS Phantom V12 having a resolution of 1280 × 800 pixels. Cameras are placed on each side of the mid-plane or in the same side of the vertical transversal planes and they are tilted by an angle of 41°. The acquisition frequency of image pairs is set to 100 Hz. Image processing is performed with DaVis 7.2.2 software from Lavision using interrogation windows of decreasing size from 64 × 64 pixels down to 16 × 16 pixels and an overlap of 50%. The final grid resolution d in each direction is 0.99 mm for the whole wake in the mid-plane and 1.08 mm for the vertical transversal planes. In average, d^* is of order of 0.014.

3. RESULTS

3.1 Underbody velocity characterization

The flow at the underbody exit is investigated by SPIV to determine the influence of porosity of the pressure loss system on the underbody flow homogeneity. Vertical profiles of velocity $\overline{u}$ at $x^* = 0.02$ are shown in Fig. 2a for selected grids over the investigated range of porosity. For porosity higher than 62%, profiles are rather symmetrical with respect to the middle of the ground clearance ($y^* = 0.13$), as expected for a channel flow; the slight deviation from symmetry for the others porosities may be attributed to differences in the boundary-layer development along the ground ($y^* = 0$) and along the model bottom ($y^* = 0.26$).

Profiles of velocity fluctuations are provided in Fig. 2b. For porosity higher than 62% the maximum of velocity fluctuations is located in the shear layer that forms at the ground clearance exit. Furthermore, the turbulence level within the ground clearance flow is rather constant as long as the pressure loss system is used. This level is higher in the case of porosity equal to 100%.

The flow velocity U_s, defined as the mean velocity spatially averaged over the ground clearance height is deduced from the velocity profiles. The evolution of the dimensionless parameter $\lambda = U_s/U_\infty$ with porosity is presented in Fig. 2c. At first order, the evolution of λ with the porosity is linear excepted without the pressure loss system. In this last case, λ is significantly smaller than unity, which is attributed to the intrinsic head losses created in the ground clearance area.

3.2 Mean pressure coefficient at the model base

The spatial and temporal average base pressure coefficient $\langle \overline{C_{p,c}} \rangle$ are presented in Fig. 3a. The evolution of $\langle \overline{C_{p,c}} \rangle$ with λ leads to the identification of four pressure classes, numbered from (I) to (IV), by values of $\langle \overline{C_{p,c}} \rangle$ nearly constant (especially for classes (II), (III) and (IV)). These classes are separated by dashed lines as an indication. Indeed, the limited number of underbody velocity configurations does not make it possible to precisely determine a boundary, if there is one, between each class.

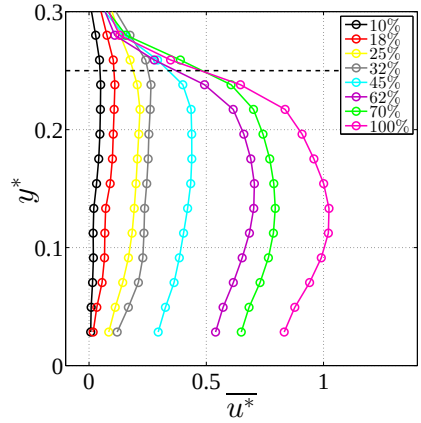

(a)

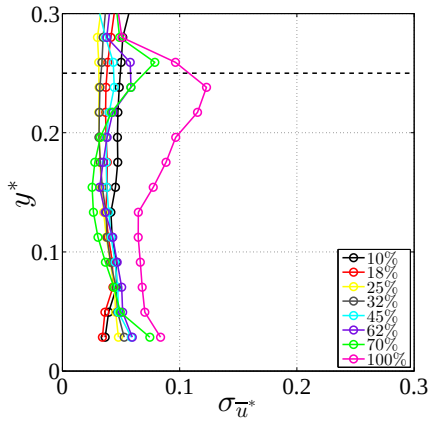

(b)

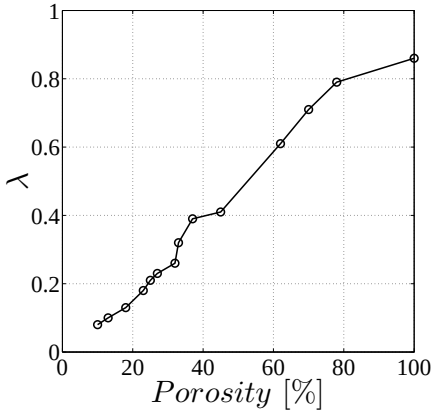

(c)

Figure 2: Profiles of mean longitudinal velocity (a) and standard deviation at $x^* = 0.02$ of the underbody flow (b) for several pressure losses (porosity is indicated in the legend). The black dashed line represents the top of the ground clearance at $y^* = 0.26$. (c) Evolution of the ratio $\lambda = U_s/U_\infty$ with the porosity.

Class (I) is characterized by an increase of the pressure coefficient for low underbody velocities, class (II) corresponds to the maximum values of $\langle\overline{C_{p,c}}\rangle$. The class (III) is associated with the lowest values of $\langle\overline{C_{p,c}}\rangle$ and class (IV) corresponds to an almost constant value of $\langle\overline{C_{p,c}}\rangle$ which is in the range of base pressure of classes (II) and (III). Sec. 3.3 will show that each class is associated with a specific structure of the near wake.

Base pressure distributions obtained for specific values of $\lambda = [0.08, 0.21, 0.39, 0.86]$ chosen in each class are presented in Fig. 3a. The pressure distribution is mainly vertically stratified and horizontal pressure gradients remain low. This result is consistent with the pressure distributions obtained with a square-back Ahmed body [2], GTS/GETS models [12, 21] or with real vehicles [3, 10].

For very small values of λ, in class (I), the pressure distribution is uniform over the entire surface of the base. For the other classes, more intense areas of low pressure are located in the lower part of the base. They are linked to the presence of a vortex structure created by the back-flow which will be described in Sec. 3.3. The evolution of the vertical pressure gradient presented in Fig. 3b allows to identify very clearly the same four classes, particularly for class (I).

Time-averaged pressure fluctuations are shown in Fig. 4. Pressure fluctuations for classes (I), (II) and (III) are much lower than those for class (IV). For this latter class, the spot of large pressure fluctuations is the sign of a global unsteadiness of the flow which may lead to a top/bottom bi-stability oscillation as observed by [8] for a ground clearance height variation.

3.3 Mean flow structure

Fig. 5 presents the streamlines in the mid-plane for the same values of λ than for the base pressure distribution presented in Fig. 3a. Two very different wake structures are identified. The first one, for $\lambda \leq 0.4$ (classes (I), (II) and (III)) is characterized by flow separation on the ground. The second one, corresponding to class (IV), is associated with a closed recirculation bubble delimited by the separation surface developing along edges of the rear base. This bubble is detached from the ground like for wakes obtained with a square-back Ahmed body [2] or a GTS/GETS model [15].

The wake of class (I) looks like the wake obtained by Chaligné et al. [6]. A small recirculation bubble is likely present near the bottom part of base created by the underbody flow detachment. However, the limits of the velocity measurements make it impossible to identify it precisely. For classes (II) and (III), the back-flow created by the underbody flow separation is now clearly apparent. The height of the stagnation point at the base, linked to this back-flow, increases between class (II) and class (III). This back-flow is responsible for the formation of a counter-rotating vortex attached to the bottom part of the base. The latter one is correlated with low pressures observed on the color maps of $\overline{C_{p,c}}$. Finally, for class (IV), the momentum of the underbody flow is high enough to avoid flow separation from the ground. The wake is then

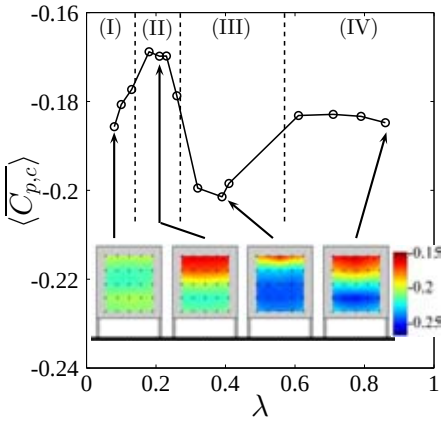

(a)

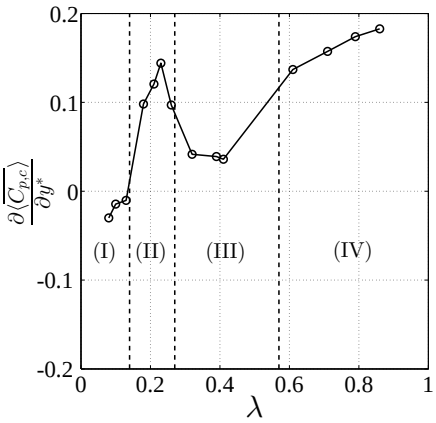

(b)

Figure 3: Evolution with λ of $\langle\overline{C_{p,c}}\rangle$ (a). Color maps of $\overline{C_{p,c}}$ on the rear base surface for selected configurations are shown. (b) Evolution with λ of the vertical pressure gradient.

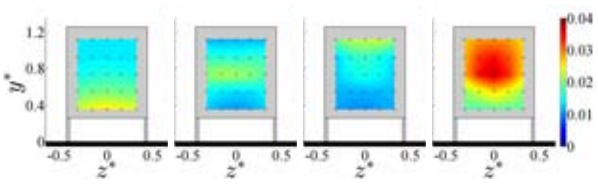

(a) (b) (c) (d)

Figure 4: Color maps of pressure fluctuations for $\lambda = 0.08$ (a), $\lambda = 0.21$ (b), $\lambda = 0.39$ (c) and $\lambda = 0.86$ (d).

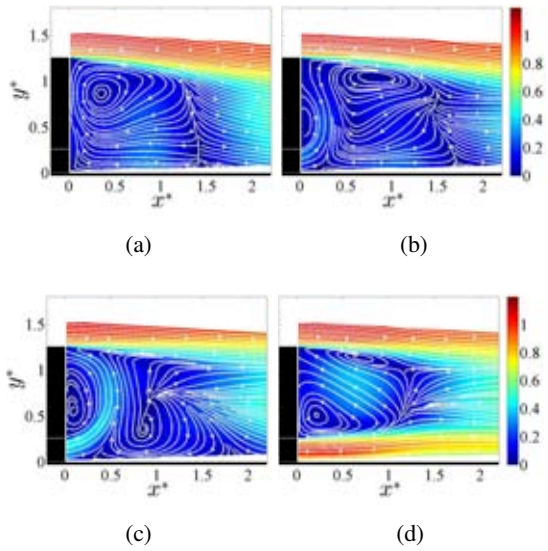

Figure 5: Non-dimensional velocity in the mid-plane for $\lambda = 0.08$ (a), $\lambda = 0.21$ (b), $\lambda = 0.39$ (c) and $\lambda = 0.86$ (d).

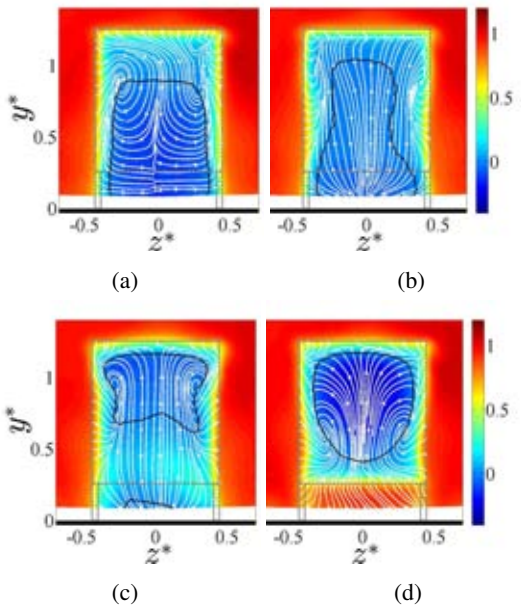

Figure 6: Streamlines and streamwise velocity magnitude in $x^* = 0.5$ for $\lambda = 0.08$ (a), $\lambda = 0.21$ (b), $\lambda = 0.39$ (c) and $\lambda = 0.86$ (d). Black line is the contour $u^* = 0$.

formed in the mid-plane by two non-symmetric counter-rotating structures.

Streamwise velocity magnitude with the streamlines of the near wake in the vertical transverse plane at $x^* = 0.5$ are presented in Fig. 6 for the same previous λ values. The streamlines make it possible to identify once again the four flow classes. The class (I) is associated with horizontal streamlines in the lower part of the near wake with a rolling-up of the streamlines in the upper part of the near wake. For classes (II) and (III), the back-flow is clearly identified over a large part of the width of the near wake by vertical streamlines. A rolling-up of the streamlines in the upper part is also observed. The classes (II) and (III) differ mainly in the size of the rolling-up and the velocity magnitude of the back-flow. For the last class, the rolling-up of the current lines is now observed in the lower part of the near wake and no negative streamwise velocity is present near the ground. The vorticity ω_x (not presented here) suggests that the streamlines rolling-up are not perpendicular to the measurement plane.

3.4 Turbulence

The turbulent kinetic energy k^*, defined by Eq. 2, is presented in Fig. 7 in the mid-plane.

$$k^* = \frac{1}{2}\frac{\overline{u'u'} + \overline{v'v'} + \overline{w'w'}}{U_\infty^2} \qquad (2)$$

The four flow classes are distinguished from one another by the location of the high turbulence areas and by their intensity. For classes (I) and (II), the maximum turbulence area is mainly located at the wake closure. A spectral analysis at this location on velocity fluctuations w' underlines the presence of a lateral vortex shedding responsible for these high k^* levels. For classes (III) and (IV), the main turbulence area is located in the vicinity of the upper shear layer. Spatial correlation and spectral analysis carried out at this location highlight the birth of Kelvin-Helmholtz instabilities which are responsible for the high k^* levels. Lateral vortex shedding is also observed at the wake closure but its intensity is damped with respect to classes (I) and (II).

The turbulent kinetic energy in the vertical transverse plane at $x^* = 0.5$ is given in Fig. 8. For all classes, the velocity fluctuations in the bottom shear layer are low compared with the velocity fluctuations in the other shear layers. For classes (I) and (II), the main velocity fluctuations are located in the lateral shear layers linked to the lateral vortex shedding. For class (III), the main velocity fluctuations are localized in the upper shear layer and are related to the back-flow impingement which disturbs the upper shear layer development. For flow class (IV), the velocity fluctuations are more homogeneously distributed over the upper and lateral shear layers. It should also be noted that turbulence is increased into a large part of the closed recirculating bubble as observed for the base pressure fluctuations in Fig. 4. This confirms the unsteadiness characteristic of the near wake which could lead to the oscillation of the flow (bi-stability phenomenon).

Thus, in function of the flow class, the turbulent areas are not located in the same place in the near wake and are not generated by the same physical phenomenon which could imply different control strategies to improve the stability of the wake.

4. DISCUSSION

The study of the streamlines in the previous section highlighted two different kinds of wake: wakes with a flow separation at the ground for flow classes (I), (II) and (III) and wakes with a closed recirculation bubble de-

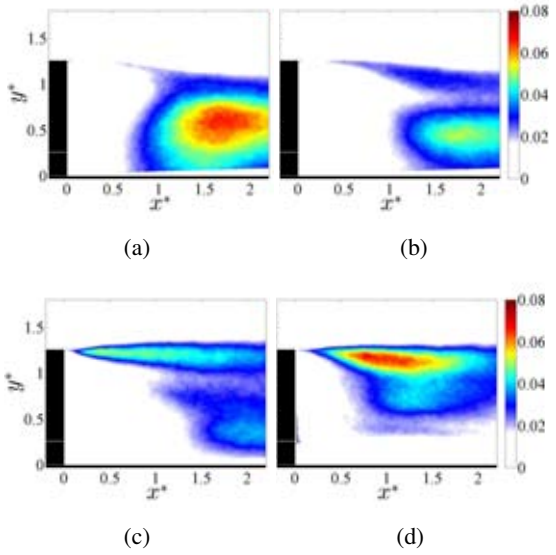

Figure 7: Non-dimensional turbulent kinetic energy k^* in the mid-plane for $\lambda = 0.08$ (a), $\lambda = 0.21$ (b), $\lambda = 0.39$ (c) and $\lambda = 0.86$ (d).

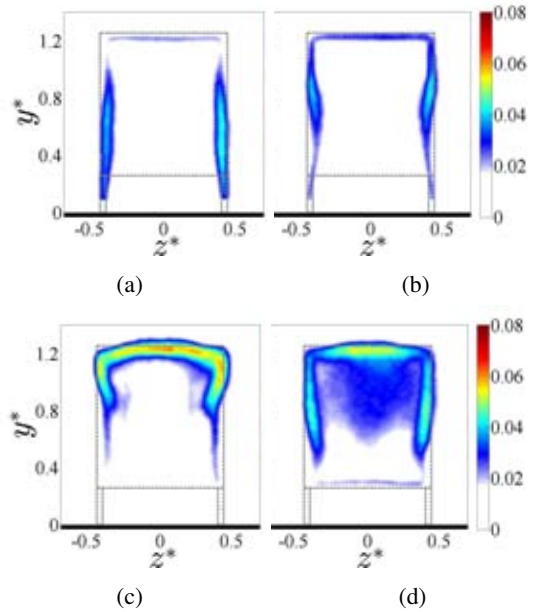

Figure 8: Non-dimensional turbulent kinetic energy k^* at $x^* = 0.5$ for $\lambda = 0.08$ (a), $\lambda = 0.21$ (b), $\lambda = 0.39$ (c) and $\lambda = 0.86$ (d). Black line is the contour $u^* = 0$.

tached from the ground for class (IV). In this section we use quantitative SPIV velocity measurements in the mid-plane to identify the four flow classes. Two analysis tools are used: a momentum balance is carried out in the lower part of the near wake and the calculation of a pressure gradient associated with the local curvature of the streamlines of the back-flow is performed.

4.1 Momentum balance

The momentum balance, given by Eq. 3 is carried out on a closed contour Ω in the mid-plane where the flow is considered 2D.

$$\sum \vec{F} = \int_{\Omega} \rho \vec{v}(\vec{v}.\vec{n}) dl \tag{3}$$

The objective is to quantify which part of the underbody momentum is convected downstream along the ground and which part is vertically directed to form a back-flow. The left boundary Ω_1 is chosen at the end of underbody channel at $x^* = 0$. The location of the right boundary Ω_2 of the domain is chosen in order to include the flow separation on the ground for the first three flow classes. Thus, the right boundary has been arbitrarily set to $x^* = 0.5$. However, similar qualitative conclusions to those presented in the following are drawn for $0.5 \leq x^* \leq 1$. The upper boundary Ω_3 is defined by the altitude of the upper wall of the underbody area $y^* = G^*$. The bottom boundary is chosen on the ground Ω_4. In this domain, the turbulence and viscous effects are negligible with respect to pressure forces. The momentum balance is projected along $\vec{x}$ and the different terms of the right-hand side of the balance are given by Eq. 4-6.

$$\zeta_1 = 2 \int_{\Omega_1} -\overline{u^*}^2 dy^* \tag{4}$$

$$\zeta_2 = 2 \int_{\Omega_2} \overline{u^*}^2 dy^* \tag{5}$$

$$\zeta_3 = 2 \int_{\Omega_3} -\bar{u^*}\bar{v^*} dx^* \tag{6}$$

The contribution ζ_4 along Ω_4 is zero due to the boundary condition. The term ζ_1 represents the amount of momentum of the underbody flow and its evolution with λ is quadratic as shown in Fig. 9a. The value of $(\zeta_1 + \zeta_2)$ is calculated to estimate the amount of momentum of the underbody flow which is preserved in $x^* = 0.5$. Finally the last quantity ζ_3 allows to quantify the $\vec{x}$ momentum of the vertical back-flow.

$(\zeta_1 + \zeta_2)$ is positive for values of λ smaller than 0.14, which shows that the momentum in Ω_2 is higher than in Ω_1. So momentum in Ω_2 can't be provided by the momentum in Ω_1. Positive values of $(\zeta_1 + \zeta_2)$ make it possible to identify wakes with a single clockwise recirculation bubble, characteristic of class (I). For values of λ in the range 0.14 to 0.51, ζ_3 increases with λ and is almost equal to $-\zeta_1$. There is a transfer of momentum between the underbody outlet and the Ω_3 boundary. This

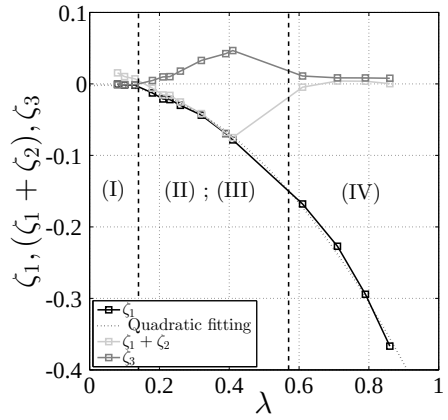

(a)

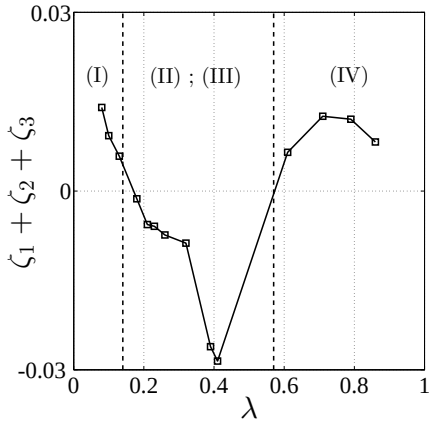

(b)

Figure 9: Evolution with λ of the different contributions to the spanwise flow of momentum balance.

is explained by the intensity of the vertical velocity in the back-flow created by the separation on the ground of the underbody flow. This characteristic then makes it possible to identify classes (II) and (III). Finally, for $\lambda > 0.51$, the decrease of ζ_3 combined with the high values of $|\zeta_1|$ shows that in the absence of back-flow, the momentum is convected from Ω_1 to Ω_2 without substantial losses. These values are characteristic of a flow with a closed recirculation bubble detached from the ground, *i.e.* a flow of class (IV).

Moreover, assuming that pressure is uniform along Ω_1 and Ω_2, the projection on $\vec{x}$ of the momentum balance is reduced to: $(P^*_{\Omega_1} - P^*_{\Omega_2})G^* = \zeta_1 + \zeta_2 + \zeta_3$. The expression $\zeta_1 + \zeta_2 + \zeta_3$ is given in Fig. 9b. The negative values of $\zeta_1 + \zeta_2 + \zeta_3$ underline the presence of an adverse pressure gradient for classes (II) and (III) responsible for the underbody flow detachment.

4.2 Curvature of the back-flow and centrifugal pressure gradient

On the basis of quantitative measured values of the velocity field, the previous momentum balance is able to differentiate three different kinds of wake: (I), (II) + (III) and (IV). However, it is not possible to differentiate classes (II) and (III). Even if streamlines in Fig. 5b and 5c show some differences (the upper clockwise vortex located downstream the counter-clockwise vortex attached to the rear base in Fig. 5b is shifted toward the ground in Fig. 5c), velocity magnitudes in this part of the near wake are very small and not sufficient to explain the large differences in mean rear base pressure observed for classes (II) and (III) in Fig. 3a. The main difference is in the magnitude of the curved jet formed by the back-flow. Therefore we focus our attention to the centrifugal pressure gradient $(\partial p/\partial n)^*$ induced by the curvature of the flow and defined by Eq. 7, with R being the local curvature radius and $\overline{V}$ the time-averaged local velocity.

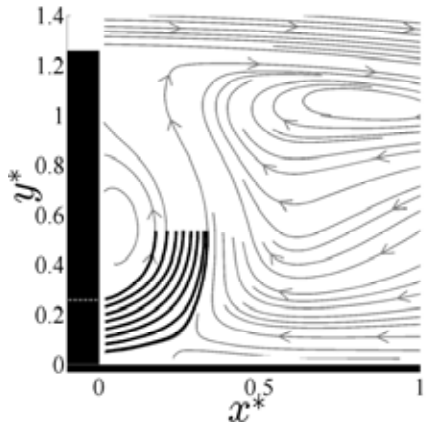

Figure 10: The centrifugal pressure gradient is calculated along the black line of each streamline.

$$\left(\frac{\partial p}{\partial n}\right)^* = |-\frac{\rho\overline{V}^2}{R} \times \frac{H}{\frac{1}{2}\rho U_\infty^2}| \tag{7}$$

The pressure gradient is computed along each steramline from the underbody outlet to the point where the streamline is vertical (see Fig. 10). The normal pressure gradient is spatially averaged along each streamline. Finally, to compare the pressure gap through the back-flow with the pressure variations at the rear base, the evolution of the mean normal pressure gradient calculated on each streamlines is then spatially averaged over the width of the back-flow estimated as the ground clearance height. The pressure jump $\Delta C_{p,jet}$ is then defined by the equation Eq. 8.

$$\Delta C_{p,jet} = \frac{1}{H}\int_0^G \langle\left(\frac{\partial p}{\partial n}\right)^*\rangle dy \tag{8}$$

A jump of $\Delta C_{p,jet}$ value is observed for $0.26 \leq \lambda \leq 0.32$ which makes it possible to differentiate classes (II) and (III). This emphasizes that characteristics (velocity and curvature) of the back-flow are decisive to distinguish classes (II) and (III).

The difference between the pressure jump through the jet of a class (II) and class (III) flow, excepted for $\lambda = 0.32$, is of the order of 0.04. By comparison, the difference of mean pressure coefficient $\langle\overline{C_{p,c}}\rangle$ between class (II) and (III) is in the order of 0.03. Thus, the drop in

pressure generated by the back-flow is directly responsible for the drop in pressure at the rear base between class (II) and class (III).

These two criteria used in this section, flow momentum and centrifugal pressure gradient are therefore efficient and relevant to differentiate the same different flow classes than the one previously identified from pressure measurements at the base. Moreover, the pressure jump through the back-flow makes it possible to qualitatively explain the intensity of the depression observed in the bottom part of the base.

5. FLOW CONTROL STRATEGIES

Several control strategies can be applied in order to increase the base pressure and thus reduce the drag force of the bluff body. The easiest strategy aims to reduce the cross-section of the wake by using a "vectoring" effect, generated for example by flaps. This aerodynamic device are effective on Ahmed bodies [9], GTS/GETS models [18] or on simplified truck geometries [7, 20]. The "vectoring" effect can be improved by combining active control with unsteady pulsed jet and passive control with flaps [6] or rounded boundaries in order to use the Coanda effect [2, 19]. Another flow control strategy is to reduce turbulence in the shear layers. Velocity fluctuations are mainly located in the upper and lateral shear layers, whatever is the class of the flow. Using passive or/and active control on the upper and lateral edges of the rear base would therefore be fully justified. The use of active flow control by periodic jets in order to decrease the turbulence in the shear layer could be used for classes (II) and (III) as it has already been effective on class (I) [6] and (IV) [2, 18]. It is important to underline that these flow control strategies for class (IV) are not dedicated to attenuate vortex shedding which do not contribute significantly to the drag force as it is explained by Greenblatt et al. [11]. Finally, more specifically for classes (I) to (III), aerodynamic devices could be set up on the lower edge of the rear base in order to increase the curvature of the back-flow. This would make it possible on the one hand to limit the low pressure generated by the curvature of the back-flow and on the other hand to take away of the rear base the vortex generated by this back-flow.

6. CONCLUSIONS

The experimental study performed has characterized the evolution of the near wake of a simplified truck model for different underbody velocities. The several underbody velocities tested are set by the use of a pressure loss system introduced into the underbody area.

Rear base pressure analysis underline a vertical stratification of pressure similar to those on scale-one industrial vehicles. Moreover, the increase in pressure fluctuations at the rear base for high underbody velocities suggests to a top/bottom bi-stability phenomenon.

The spatial and time-averaged base pressure and the vertical pressure gradient make it possible to distinguish four flow classes. The first three flow classes ($\lambda \leq 0.4$) are characterized in the mid-plane with a recirculation bubble attached to the ground. The wake of class (I), corresponding to the lowest λ values, is characterized in the mid-plane by a single vortex. The wake of classes (II) and (III) is characterized by a back-flow impinging the rear base. This kind of wake is typical of industrial vehicles. The last class ($\lambda \geq 0.6$) is associated with a close wake detached from the ground. The wake looks like that of an Ahmed body or on GTS/GETS models.

Two analytical tools are then used to determine this classification using the mean velocity data in order to associate the rear base pressure to a wake structure. A momentum balance is performed at the underbody outplet in order to quantify how the underbody momentum is spread into the near wake. This momentum balance is efficient to distinguish three classes over four. The second tool, complementary to the first one, concerns the analysis of the characteristics of the back-flow with the calculation of a centrifugal pressure gradient. This tool makes it possible to make a clear distinction between the classes (II) and (III) and clearly shows that the depression observed at the bottom of the rear base is directly associated with the curvature and the velocity of the back-flow. Thus, for the three first classes, it would be interesting to increase the curvature of the back-flow to limit the low pressure zone and then to reduce the drag coefficient.

These classes are also associated with a different near wake dynamics. For class (I) and (II), the transverse velocity fluctuations located at the closure of the wake mainly contribute to the turbulent kinetic energy. They are associated with the presence of a lateral vortex shedding. This vortex shedding is also detected for classes (III) and (IV) but its intensity is damped. For these two classes, longitudinal and vertical velocity fluctuations are mainly located in the vicinity of the upper shear layer. These velocity fluctuations are related to Kelvin-Helmholtz instabilities generated by the back-flow impinging the shear layer. These various distributions of turbulence suggest that it would be difficult to implement a universal flow control solution.

REFERENCES

[1] S.R. Ahmed, G. Ramm, and G. Faitin. Some salient features of the time-averaged ground vehicle wake. Technical Report 840300, SAE, 1984.

[2] D. Barros, J. Borée, B.R. Noack, A. Spohn, and T. Ruiz. Bluff body drag manipulation using pulsed jets and coanda effect. *Journal of Fluid Mechanics*, 805:422–459, 10 2016.

[3] O. Cadot, A. Courbois, D. Ricot, T. Ruiz, F. Harambat, V. Herbert, R. Vigneron, and J. Délery. Characterizations of force and pressure fluctuations on real vehicles. *International Journal of Engineering Systems Modelling and Simulation*, 8(2):99–105, 2016.

[4] O. Cadot, A. Evrard, and L. Pastur. Imperfect supercritical bifurcation in a three-dimensional turbulent wake. *Physical Review E*, 91(6):063005, 2015.

[5] S. Chaligné. *Contrôle du sillage d'un corps non profilé: application expérimentale à une maquette simplifiée de véhicule industriel*. PhD thesis, Ecully, Ecole centrale de Lyon, 2013.

[6] S. Chaligné, T. Castelain, M. Michard, and D. Juvé. Experimental application of active flow control on a 1:8 scale, simplified truck model. In *Aerovehicles 1*, 2014.

[7] A. Devesa and T. Indinger. Fuel consumption reduction by geometry variations on a generic tractor-trailer configuration. *SAE International Journal of Commercial Vehicles*, 5(2012-01-0105):18–28, 2012.

[8] M. Grandemange, M. Gohlke, and O. Cadot. Bistability in the turbulent wake past parallelepiped bodies with various aspect ratios and wall effects. *Physics of Fluids*, 25(9):095103, 2013.

[9] M. Grandemange, A. Mary, M. Gohlke, and O. Cadot. Effect on drag of the flow orientation at the base separation of a simplified blunt road vehicle. *Experiments in fluids*, 54(5):1529, 2013.

[10] M. Grandemange, D. Ricot, C. Vartanian, T. Ruiz, and O. Cadot. Characterisation of the flow past real road vehicles with blunt afterbodies. *International Journal of Aerodynamics*, 24(1-2):24–42, 2014.

[11] D. Greenblatt and I.J. Wygnanski. The control of flow separation by periodic excitation. *Progress in Aerospace Sciences*, 36(7):487–545, 2000.

[12] W.T. Gutierrez, B. Hassan, R.H. Croll, and W.H. Rutledge. Aerodynamics overview of the ground transportation systems (gts) project for heavy vehicle drag reduction. Technical Report 960906, SAE, 1996.

[13] M. Lenngren and C. Håkansson. Cfd analysis of aerodynamic trailer devices for drag reduction. Master's thesis, Chalmers University of Technology, 2010.

[14] K.H. Lo and K. Kontis. Flow characteristics over a tractor-trailer model with and without vane-type vortex generator installed. *Journal of Wind Engineering and Industrial Aerodynamics*, 159:110–122, 2016.

[15] D. McArthur, D. Burton, M. Thompson, and J. Sheridan. On the near wake of a simplified heavy vehicle. *Journal of Fluids and Structures*, 66:293–314, 2016.

[16] S. Pellerin, B. Podvin, and L. Pastur. Characterization of the near-wake of an ahmed body profile. *World Academy of Science, Engineering and Technology, International Journal of Mechanical, Aerospace, Industrial, Mechatronic and Manufacturing Engineering*, 10(5):829–834, 2016.

[17] K. Salari, J. Ortega, and P. Castellucci. *Computational prediction of aerodynamic forces for a simplified integrated tractor-trailer geometry*. United States. Department of Energy, 2004.

[18] H.J. Schmidt, R. Woszidlo, C.N. Nayeri, and C.O. Paschereit. Drag reduction on a rectangular bluff body with base flaps and fluidic oscillators. *Experiments in Fluids*, 56(7):1–16, 2015.

[19] A. Seifert, T. Shtendel, and D. Dolgopyat. From lab to full scale active flow control drag reduction: How to bridge the gap? *Journal of Wind Engineering and Industrial Aerodynamics*, 147:262–272, 2015.

[20] M. Szmigiel, T. Castelain, M. Michard, D. Chacaton, and D. Juvé. Impact of the underside velocity on the drag reduction of a trailer model using a passive control system. In *Aerovehicles 2*, 2016.

[21] G.M.R. Van Raemdonck, P. Van Leeuwen, and M.J.L. Van Tooren. Comparison of experimental and numerically obtained flow properties of a bluff body. In *The Aerodynamics of Heavy Vehicles III*, pages 393–411. Springer, 2016.

[22] G.M.R. Van Raemdonck and M.J.L. Van Tooren. Time averaged phenomenological investigation of a wake behind a bluff body. In *Bluff Body Aerodynamics and Application VI Conference, Milan, Italy*, 2008.

Anne VENABLES
3AF Executive Secretary
Phone: +33 1 56 64 12 30
Email: secr.exec@aaaf.asso.fr

Information available on:
www.3af-aerodynamics2017.com